HOKKAIDO UNIVERSITY

Title	Inverse analysis of anisotropy of solid-liquid interfacial free energy based on machine learning
Author(s)	Kim, Geunwoo; Yamada, Ryo; Takaki, Tomohiro; Shibuta, Yasushi; Ohno, Munekazu
Citation	Computational materials science, 207, 111294 https://doi.org/10.1016/j.commatsci.2022.111294
Issue Date	2022-05
Doc URL	http://hdl.handle.net/2115/92149
Rights	©2022. This manuscript version is made available under the CC-BY-NC-ND 4.0 license http://creativecommons.org/licenses/by-nc-nd/4.0/
Rights(URL)	http://creativecommons.org/licenses/by-nc-nd/4.0/
Type	article (author version)
File Information	2022Kim_ISD-CNN_manuscript_HUSCAP.pdf

Inverse analysis of anisotropy of solid-liquid interfacial free energy based on machine learning

Geunwoo Kim[a], Ryo Yamada[b], Tomohiro Takaki[c], Yasushi Shibuta[d] and
Munekazu Ohno[b,*]

[a] *Graduate School of Engineering, Hokkaido University, Kita13 Nishi8, Kita-ku, Sapporo, Hokkaido 060-8628, Japan*

[b] *Division of Materials Science and Engineering, Faculty of Engineering, Hokkaido University, Kita13 Nishi8, Kita-ku, Sapporo, Hokkaido 060-8628, Japan*

[c] *Faculty of Mechanical Engineering, Kyoto Institute of Technology, Matsugasaki, Sakyo-ku, Kyoto 606-8585, Japan*

[d] *Department of Materials Engineering, The University of Tokyo, 7-3-1 Hongo, Bunkyo-ku, Tokyo 113-8656, Japan*

* Corresponding author: mohno@eng.hokudai.ac.jp

Abstract:

A machine leaning-based approach is proposed for the inverse analysis of the anisotropy parameters of solid-liquid interfacial free energy. The interface shape distribution (ISD) map, which characterizes the details of the dendrite morphology, was selected as the input of a convolutional neural network (CNN). The ISD maps for a free-growing dendrite during the isothermal solidification of a model alloy system were obtained by quantitative phase-field simulations and used as the training and test data for the CNN. Two anisotropy parameters were estimated with errors of less than 5 %, which can be further improved by increasing the size of the training dataset.

Keywords:

solid-liquid interfacial free energy, anisotropy, interface shape distribution, phase-field simulation, machine learning

1. Introduction

A dendrite is a typical shape of crystals growing in an undercooled melt. Its morphology is largely determined by the anisotropy of the solid-liquid interfacial free energy in most metallic systems because of negligible interfacial attachment kinetics. The anisotropy is essential information required for understanding and controlling the solidification microstructures [1]. Experimental determination of the anisotropy with high accuracy is one of an important and long-standing concern in the field of solidification science and engineering.

For crystals with cubic symmetry, the interfacial free energy is expressed as follows [2]:

$$\gamma(\boldsymbol{n}) = \gamma_0[1 + \varepsilon_1(Q_1 - 3/5) + \varepsilon_2(3Q_1 + 66Q_2 - 17/7)] \qquad (1)$$

where γ_0 is the average solid-liquid interfacial free energy, $\boldsymbol{n}$ is the unit vector normal to the crystal plane of the interface, $Q_1 = n_x^4 + n_y^4 + n_z^4$, $Q_2 = n_x^2 n_y^2 n_z^2$, and n_i are the Cartesian components of $\boldsymbol{n}$. The anisotropic property of $\gamma(\boldsymbol{n})$ is characterized by two anisotropy parameters, ϵ_1 and ϵ_2, which are the main concern in this study. Considering that the values of ϵ_1 and ϵ_2 determine the preferential growth orientation of the crystal, the dendrite structure largely depends on these values. To be specific, the crystal preferentially grows in the <100> orientation when ϵ_1 is dominant, whereas it preferentially grows in the <110> orientation when ϵ_2 is dominant. The values of ϵ_1 and ϵ_2 vary from element to element [3]. Furthermore, ϵ_1 and ϵ_2 in an Al-rich fcc solid solution were found to change with the Zn concentration in Al-Zn alloys [4]. The growth mode of the fcc dendrite changed from <100> to the hyperbranched and <110> growth mode as the Zn concentration increased. A similar behavior was also observed in Al-Sm alloys [5]. In addition, computational work based on molecular dynamics (MD) simulations showed that the anisotropy strength of $\gamma(\boldsymbol{n})$ is temperature dependent [6]. Therefore, the values of ϵ_1 and ϵ_2 are required for different solidification conditions and alloy concentrations to predict and control the dendrite structure.

To experimentally determine $\gamma(\boldsymbol{n})$, an equilibrium shape of the solid under well-controlled solidification conditions must be first realized, and then the solid-liquid interface region should be imaged with enough accuracy to elucidate a few percent difference of $\gamma(\boldsymbol{n})$ in metallic systems [7]. The experimental measurement of $\gamma(\boldsymbol{n})$ has been seldomly reported owing to these difficulties. Atomistic simulations, such as MD simulations, are effective in determining $\gamma(\boldsymbol{n})$ [3]. The capillary fluctuation method [8] and cleaving technique [9] were developed for computing $\gamma(\boldsymbol{n})$ from MD simulations. These methods have been successfully applied to several types of materials. Moreover, a

new approach for computing $\gamma(\boldsymbol{n})$ based on MD simulation was recently developed by the present authors' group using a data assimilation technique [6, 10]. These approaches are considered powerful and effective. However, the accuracy of MD simulations largely depends on the accuracy of the atomic potential, which is not always sufficiently high to produce reliable results especially in alloy systems. Hence, the development of new experimental techniques that could resolve the above-mentioned difficulties is in high demand.

X-ray imaging techniques have enabled the in-situ observation of dendritic growth in thin samples, and have made significant progress [11−15]. Moreover, X-ray tomographic microscopy recently revealed the time evolution of the three-dimensional (3D) morphology of solidification microstructures in bulk samples [16−19]. One can expect that the in-situ observation techniques can be applied to the estimation of $\gamma(\boldsymbol{n})$. Note that $\gamma(\boldsymbol{n})$ cannot be directly elucidated from the growing shape observed in the in-situ observation because it is not an equilibrium shape. One way to determine $\gamma(\boldsymbol{n})$ from the in-situ observation is to compare the 3D dendrite structures obtained from the experiment and simulation with the assumed values of ϵ_1 and ϵ_2, which are estimated in a trial-and-error manner. However, in this method, all information, such as the crystallographic orientation of the solid and initial concentration field, except for ϵ_1 and ϵ_2, must be provided in the simulation, which is generally a demanding task. In this study, we focused on the inverse analysis of ϵ_1 and ϵ_2 using easy-to-handle information closely associated with the anisotropy of $\gamma(\boldsymbol{n})$ instead of the direct use of the 3D microstructure. An interface shape distribution (ISD) map [18, 20] was considered suitable for this purpose. The 3D dendrite morphology can be characterized by the local morphology of the interface and its statistical properties. The ISD map shows the existing probability or frequency of the local morphology of the interface, described by the shape factor and curvedness [18], which will be explained later. Considering that the ISD map contains essential information of the 3D dendrite morphology, one may expect a unique relationship between the ISD map and a set of ϵ_1 and ϵ_2. In this case, ϵ_1 and ϵ_2 can be estimated from the ISD map obtained in the in-situ observation or other experimental techniques, such as serial sectioning of the quenched sample.

In this study, we investigated the feasibility of the aforementioned inverse analysis approach. First, the ISD maps for dendrite morphologies associated with different values of ϵ_1 and ϵ_2 were obtained from the quantitative phase-field simulations. Then, machine learning was applied to describe the relationship between the ISD map and a set of ϵ_1 and ϵ_2. The machine learning model allow the ϵ_1 and ϵ_2 set to be estimated from a given ISD map. Details of the phase-field simulations,

computational conditions for dendrite growth, and machine learning are explained in the following section. The results and discussion are presented in Section 3, followed by the conclusions in the final section.

2. Methods

2.1. Quantitative phase-field model

The phase-field model is a diffuse-interface approach in which explicit tracking of the position of moving interface can be avoided and, also, the shape of the curved interface can be smoothly and precisely expressed [21–23]. Importantly, the quantitative phase-field model developed based on the thin-interface asymptotics exactly recovers the free-boundary problem within the framework of the diffuse-interface [23–29], thereby serving as an effective and reliable tool of numerical experiment for investigating solidification microstructures [30]. In this study, we performed quantitative phase-field simulations for a free-growing 3D dendrite during isothermal solidification of a dilute binary alloy.

The phase-field variable ϕ takes $+1$ in the solid and -1 in the liquid and it varies between these values continuously inside the solid-liquid interface. Instead of directly solving the time evolution of ϕ, we solved the following time evolution equation of $\psi = \sqrt{2} \tanh^{-1} \phi$ according to the preconditioning technique [31]:

$$
\begin{aligned}
\alpha \eta^2 a_s(\boldsymbol{n})^2 &[1 + (1-k)u]\frac{\partial \psi}{\partial t} \\
&= \eta^2 \nabla[a_s(\boldsymbol{n})^2] \cdot \nabla\psi + \eta^2 a_s(\boldsymbol{n})[\nabla\psi^2 - \sqrt{2}\phi|\nabla\psi|^2] \\
&\quad + \eta^2 \sum_{r=x,y,z} \partial_r \left(|\nabla\psi|^2 a_s(\boldsymbol{n})\frac{\partial a_s(\boldsymbol{n})}{\partial \psi_r}\right) \\
&\quad - \sqrt{2}\eta^2 \phi a_s(\boldsymbol{n})|\nabla\psi|^2 \sum_{r=x,y,z} \psi_r \frac{\partial a_s(\boldsymbol{n})}{\partial \psi_r} + \sqrt{2}\phi \\
&\quad - \sqrt{2}\lambda(1-\phi^2)u
\end{aligned}
\tag{2}
$$

where $\eta = W_0/d_0$, with d_0 denoting the chemical capillary length and W_0 the interface thickness, and $\alpha = D_l\tau_0/W_0^2$ with D_l denoting the liquid diffusivity, and the phase-field relaxation time $\tau_0 = a_2\lambda W_0^2/D_l$. Here, $\lambda = a_1\eta$ is the coupling constant, $a_1 = 0.8839$, and $a_2 = 0.6267$. $a_s(\boldsymbol{n})$ is given as $a_s(\boldsymbol{n}) = 1 + \varepsilon_1(Q_1 - 3/5) + \varepsilon_2(3Q_1 + 66Q_2 - 17/7)$. The dimensionless supersaturation is defined by $u = (c_l - c_l^e)/(c_l^e - c_s^e)$ where c_l is the liquid concentration, and c_l^e and c_s^e represent the equilibrium concentrations of the liquid and solid, respectively. The time evolution

4

equation of u is given as:

$$\frac{1+k-(1-k)\phi}{2}\frac{\partial u}{\partial t}$$

$$= \nabla$$

$$\cdot\left[q(\phi)\nabla u + a_{AT}\eta[1+(1-k)u]\frac{(1-\phi^2)}{\sqrt{2}}\frac{\partial\psi}{\partial t}\frac{\nabla\psi}{|\nabla\psi|}\right] \quad (3)$$

$$+\frac{1}{2\sqrt{2}}[1+(1-k)u](1-\phi^2)\frac{\partial\psi}{\partial t}-\nabla\cdot J_{noise}$$

where k is the equilibrium partition coefficient, $a_{AT} = (1-q_s)/2\sqrt{2}$ with $q_s = kD_s/D_l$, and $q(\phi) = [(1+\phi)q_s + (1-\phi)]/2$. J_{noise} represents the fluctuation of the solute flux.

By solving Eqs. (2) and (3), one can reproduce the free-boundary problem for isothermal solidification in a dilute binary alloy, that is, solute diffusion in the bulks, solute conservation at the moving interface, and the Gibbs-Thomson effect [26]. Note that the length and time scales in Eqs. (2) and (3) were normalized by d_0 and d_0^2/D_l, respectively. Thus, except for the two anisotropy parameters ϵ_1 and ϵ_2, the growth problem in this system depends only on three parameters, namely k, q_s, and initial supersaturation of u.

2.2 Computational conditions

Equations (2) and (3) were discretized using a second-order finite-difference scheme for space. Time integration was performed using the first-order Euler scheme. To reduce the computational cost, only one-eighth of the system was considered by applying mirror boundary conditions to the x-y plane at z = 0, y-z plane at x = 0, and z-x plane at y = 0 of the computational domain. The zero-flux boundary condition was employed on the x-y plane at z = L_{sys}, y-z plane at x = L_{sys}, and z-x plane at y = L_{sys}, where L_{sys} represents the system size. An initial solid seed was placed at the origin of the 3D computational domain occupied by the liquid phase to simulate a free-growing dendrite under isothermal conditions.

In this study, we focused on a model alloy system with $k = 0.1$ and $q_s = 10^{-4}$. The computational domain was discretized into 512^3 grid points. The normalized grid spacing Δx was set to 13 and η was set as $1.2\Delta x$. The initial supersaturation was set as $u_0 = -0.3$. The step size of the normalized time was set as $\Delta t = 24.14$, and all simulations were performed until $t = 50,000\Delta t$. These values were selected to achieve a balance between the accuracy and computational cost in the preliminary simulations. The free growth without interaction with the boundaries of the domain was realized for

all values of ϵ_1 and ϵ_2 examined in this study until $t = 50,000\Delta t$. All computations were accelerated using graphics processing units.

2.3 Interface shape distribution (ISD)

The morphology of the entire dendrite can be characterized by the statistical nature of the local interface morphology described in terms of curvedness C (called curvature in Ref. [18]) and shape factor S[32]. C is the root mean square of the principal curvatures, expressing the degree to which the interface is curved, and is defined as follows:

$$C = \sqrt{\frac{\kappa_1^2 + \kappa_2^2}{2}} \tag{4}$$

where κ_1 and κ_2 are the maximum and minimum curvatures, respectively, of the local interface. S represents the shape of the interface as follows:

$$S = \frac{2}{\pi}\tan^{-1}\left(\frac{\kappa_1 + \kappa_2}{\kappa_1 - \kappa_2}\right) \tag{5}$$

The interfaces with $S = \pm 1, \pm 0.5$ and 0 correspond to the spherical, cylindrical, and saddle point shapes, respectively, and the sign of S indicates the convex direction of the interface. The principal curvatures were obtained from the mean and Gaussian curvature, and the calculation procedure of the mean and Gaussian curvature is described in Appendix.

Fig. 1 shows an example of the dendrite at $t = 40,000\Delta t$ simulated for $(\epsilon_1, \epsilon_2) = (0.1, 0)$. The local interface of the dendrite is colored according to the values of (a) $C/\langle C \rangle$ and (b) S. Here, $\langle C \rangle$ represents the average curvedness at a given time. C exhibits high values at the tip and edges of the primary and secondary arms. S takes $+1, +0.5$, and -0.5 at the tip of the arms, edges of the secondary arms, and primary arm trunks (or roots of the secondary arm), respectively. The existing probability of the local morphology of the interface is summarized in the ISD map (Fig. 1(c)). As will be explained later, the details of the 3D dendrite morphology are represented by this 2D map. The relation between the morphology of local interface and the values of C and S in the ISD map can be found in Fig. 1 of Ref. [20]. In this study, the ISD map was calculated from the spatial distribution of ψ every $500\Delta t$. Hence, 100 ISD maps were obtained from the phase-field simulation for each set of ϵ_1 and ϵ_2. Because more than 99% of the interface area was included in the range of $C/\langle C \rangle = [0, 4]$ and $S = [-1, 1]$, all ISD maps will be presented in this range.

2.4 Deep learning by convolutional neural network (CNN)

Deep learning was utilized in this study to develop an approach for the inverse analysis of ϵ_1 and ϵ_2 from the ISD map. We employed a CNN, an artificial neural network variant suitable for processing data, which has a grid topology structure, and has been applied to image recognition, classification, segmentation etc. The CNN typically consists of three layers, namely, convolutional, pooling, and fully connected layers. The convolution layer performs a sliding dot product of the convolution kernel with the input matrix of the layer. The convolutional kernel is a matrix consisting of learnable parameters, and the convolution operation produces feature maps that are utilized as the input of the next layer. The learnable parameters are trained to decrease the loss function, such as the mean squared error (MSE) between the training data and predicted values. A pooling layer is used to reduce the dimensions of the matrix. The most common layer is the max-pooling layer, which selects the maximum value from each local components of the matrix. The fully connected layer connects every input value to each output value in the next layer, similar to a multi-layer perception neural network. The prediction accuracy of the CNN depends on how these layers are stacked and should generally increase with increasing depth of the model, i.e., the number of layers. Further details on CNNs can be found in [33–35].

The CNN architecture is presented in Fig. 2. The input image is the ISD map with a size of $128 \times 128 \times 1$, followed by three operations, each consisting of two convolution layers with a $(3,3)$ kernel size, a zero-padding and 1 stride and 1 max-pooling layer of $(2,2)$, one fully connected layer, and the output layer for continuous values of ϵ_1 and ϵ_2. Here, $(3,3)$ and (2.2) represents the size of matrix employed for convolution and max-pooling, respectively. These sizes and the number of layers, etc. are called hyperparameters that affect the accuracy of machine learning model. These hyperparameters were tuned using the validation dataset as described later. We employed a machine learning framework known as PyTorch 1.7.0. Adam and MSE were selected as the optimizer and loss function, respectively. The learning rate was set to 10^{-5} and the training was performed for 1000 epochs that was determined based on a balance between the reduction of MSE and overfitting. A typical curve of MSE vs. epochs is shown in the Supplemental data.

For the training, we used four datasets consisting of 49, 100, 196 and 400 sets of ϵ_1 and ϵ_2, which were uniformly sampled from the range of $\epsilon_1 = [0, 0.1]$ and $\epsilon_2 = [-0.01, 0]$, as shown in Fig. 3. As described in the preceding sections, the quantitative phase-field simulation of the free growth of a single dendrite under isothermal conditions was performed for each set of ϵ_1 and ϵ_2 until $t = 50,000\Delta t$ and the ISD maps were

calculated every $500\Delta t$. Namely, 100 ISD maps were obtained for each set of ϵ_1 and ϵ_2. Hence, the training datasets used in this study consisted of 4900, 10000, 19600, 40000 ISD maps. We split the training dataset into two subsets; one was used for training and the other was used for tuning the hyperparameters. The latter set is called the validation dataset. We used 80 % of the training data for training and 20 % for validation. The test dataset was obtained by randomly sampling 100 sets of ϵ_1 and ϵ_2 as shown in Fig. 3. Note that the region of $\epsilon_1 < 0.01$ or $\epsilon_2 > -0.001$ was avoided when sampling the test data. This is because the preliminary tests showed that estimations in this region involve large errors, and these values of ϵ_1 and ϵ_2 are not commonly observed in metallic systems [3]. Because the ISD maps of the test data were obtained every $500\Delta t$ for each set of ϵ_1 and ϵ_2, the test dataset consisted of a total of 10000 ISD maps. Since the test data were not employed to construct the CNN model including the hyperparameters, the generalization error can be estimated using the test dataset.

3. Results and discussion
3.1 Growth morphologies and ISD maps

The time evolution of the dendrite structure and corresponding ISD map are shown in Fig. 4. These are the results for $(\epsilon_1, \epsilon_2) = (0.1, 0)$. Starting from the initial spherical shape, the solid exhibits a dendritic structure with well-developed primary arms at $t = 10,000\Delta t$. In the ISD map at $t = 10,000\Delta t$, several peaks appear at $S \cong 0.5$, which mainly originate from the interfaces at the edges of the primary arms. The high probabilities at $C/\langle C \rangle \cong 0$ and $S \cong -0.5$ are associated with the side surface of the primary arms. In addition, the secondary arms begin to appear at $t = 10,000\Delta t$ and were well developed at $t = 40,000\Delta t$, with a dominant contribution in the ISD map.

As reported in early studies [4, 36], different growth modes arise depending on the values of ϵ_1 and ϵ_2. The dendrite structures via different growth modes and the corresponding ISD maps at $t = 40,000\Delta t$ are shown in Fig. 5, where the <100> growth simulated for $(\epsilon_1, \epsilon_2) = (0.1, 0)$, hyperbranched growth for $(\epsilon_1, \epsilon_2) = (0.05, -0.005)$, and <110> growth for $(\epsilon_1, \epsilon_2) = (0, -0.01)$ are compared. The growth morphology is very different owing to the values of ϵ_1 and ϵ_2. Importantly, there are clear differences between the ISD maps, indicating that the different values of ϵ_1 and ϵ_2 yield the difference in the ISD map. Fig. 6 shows the ISD maps at $t = 40,000\Delta t$ for different values of ϵ_1 and ϵ_2 indicated in the orientation selection map (center), where the regions of <100> growth, <100>-like hyperbranched growth, <110>-like hyperbranched growth, and <110> growth are specified according to the previous work [36]. Although the difference is not always salient, the ISD maps differ according to the values of ϵ_1

and ϵ_2. This result supports the feasibility of the proposed approach.

3.2 Estimation of anisotropy parameters

Fig. 7 shows the estimation results for ϵ_1 and ϵ_2. In all the figures, the horizontal and the vertical axes represent the true value and that estimated by the machine learning model, respectively. The dashed (diagonal) line is shown for a visual aid to indicate the agreement between them. When the amount of training data is small, the accuracy is not high. However, the accuracy is improved by increasing the amount of training data. Table 1 shows the averages of the relative and absolute errors. The error for ϵ_2 is always larger than that for ϵ_1. Importantly, both ϵ_1 and ϵ_2 can be estimated with errors of less than 5 % when employing the training dataset with 40000 maps. The accuracy is expected to further increase by increasing the size of the training dataset. Moreover, as a first attempt, we sampled the values of (ϵ_1, ϵ_2) uniformly from the range of $\epsilon_1 = [0, 0.1]$ and $\epsilon_2 = [-0.01, 0]$ to obtain the training dataset. However, higher accuracy can be probably achieved by biased sampling of (ϵ_1, ϵ_2). This point should be further investigated in a future work.

In the present approach, the ISD maps for different timesteps were utilized as the training data for each set of ϵ_1 and ϵ_2. Hence, ϵ_1 and ϵ_2 can be inversely estimated from the ISD map at any given time step. However, the accuracy of the estimation depends on the time at which the ISD map is obtained. The mean relative errors between the test data and estimated values were calculated every $500\Delta t$ for all sets of ϵ_1 and ϵ_2, which is given as:

$$\Delta E_i(t) = \frac{1}{m} \sum_j^m \left| \frac{\epsilon_i^{est,j}(t) - \epsilon_i^{true,j}}{\epsilon_i^{true,j}} \right| \tag{6}$$

where $\Delta E_i(t)$ is the mean relative error of ϵ_i at t, $\epsilon_i^{est,j}(t)$ is the estimated value of ϵ_i from the ISD map at t associated with j^{th} data in the test dataset, $\epsilon_i^{true,j}$ is the corresponding true value and m is the total number of ISD maps at each time step. Fig. 8(a) shows the dependence of the relative errors on time for the training dataset with 40000 maps. Both errors are relatively low in the period between approximately $5000\Delta t$ and $15000\Delta t$, as indicated by the vertical dashed lines. As is understood from Fig. 4, the ISD map is mainly determined by the growing shape of the primary arms during this period. The snapshots of microstructure and ISD maps during this period are provided in the Supplemental data. Note that the value of (ϵ_1, ϵ_2) determines the preferential growth direction (PGD) of dendrite, and the primary arms of free-growing dendrite exactly grow in the PGD. However, the growth direction of secondary arms may deviate from the PGD

9

due to the overlapping of solute diffusion layer of neighboring secondary arms. Therefore, the ISD maps related to the growth of primary arms are more sensitive to the change of (ϵ_1, ϵ_2) than those related to the growth of both primary and secondary arms. Accordingly, the former ISD maps are more suitable for estimation of (ϵ_1, ϵ_2) than the latter ISD maps.

The values of $5000\Delta t$ and $15000\Delta t$ discussed above must depend on the initial supersaturation and alloy systems. Hence, it should be desirable to employ a different measure indicating the condition for accurate estimation. Since the present discussion is closely related to the morphology of dendrite, we chose the surface area per unit volume of solid S_v which has often been employed as a measure characterizing the whole morphology of dendrites in a general way. Fig. 8(b) shows the time change of the reciprocal of S_v calculated for $(\epsilon_1, \epsilon_2) = (0.1, 0), (0, -0.01)$ and $(0.05, -0.005)$. In all cases, S_v^{-1} is lower than 300 during the period for accurate estimation. This value can be used as an approximate guide to obtain an accurate estimation using the proposed approach, though its validity and accuracy must be investigated in a future work.

Realizing the free growth of a dendrite during in-situ observations for long period of time is generally complicated because the effects of other dendrites and mold walls become non-negligible. Therefore, the results shown in Fig. 8 are favorable in terms of the actual application of the proposed approach. We emphasize that the application of the present approach is not limited to this time period. As shown in Fig. 8(a), a relative error of less than 10% can be expected for the ISD map in any time period tested. The error of less than 10 % is considered low because errors of 10-50 % are often involved in conventional approaches for estimation of anisotropy parameters [7]. More importantly, the accuracy of the present approach can be further improved by increasing the amount of training data.

In this study, the training data were limited to $u_0 = -0.3$. Because the orientation selection map shown in Fig. 5 is affected by the value of u_0 [36], further studies should be aimed at including the data for different initial supersaturations. The present approach should also be applied to different solidification conditions, such as continuous cooling and directional solidification. In addition, the estimation accuracy for different alloys, with different values of k and q_s and multicomponent alloys, need to be examined. Above all, the validity and efficacy of the present approach using real ISD map obtained by in-situ observation or other experimental techniques remain to be investigated in a future work.

4. Conclusions

In this study, we proposed a machine learning-based approach for the inverse analysis of anisotropy parameters of solid-liquid interfacial free energy. The ISD map, which characterizes the details of the dendrite morphology, was selected as the input for machine learning. We tested the feasibility of this approach by performing quantitative phase-field simulations for a free-growing 3D dendrite during isothermal solidification of a model alloy system to obtain training and test data. Both ϵ_1 and ϵ_2 were estimated with reasonable accuracy, which can be further improved by increasing the size of the training dataset.

The ISD map provides important information representing the details of the 3D dendrite morphology in a 2D space. The features of this map, such as the existence of a steady-state distribution, are currently an important research topic. The proposed inverse analysis approach fully exploits this 2D information and simultaneously extends its utility. We believe that the proposed approach will be helpful for advancing both numerical and experimental techniques to elucidate the formation processes of solidification microstructures.

Data availability statement

The raw/processed data required to reproduce these findings cannot be shared at this time due to technical or time limitations.

Appendix. Calculation of curvatures from phase-field profile

As described in Section 2.3, C and S were computed from the principal curvatures, κ_1 and κ_2. These principal curvatures are related to the mean curvature H and Gaussian curvatures G as:

$$H = \frac{\kappa_1 + \kappa_2}{2} \tag{A1}$$

$$G = \kappa_1 \kappa_2 \tag{A2}$$

H and G can be calculated from the signed distance function φ as [37]:

$$
\begin{aligned}
H = \frac{1}{2|\nabla\varphi|^3} &\left[\varphi_x^2(\varphi_{yy} + \varphi_{zz}) + \varphi_y^2(\varphi_{xx} + \varphi_{zz}) + \varphi_z^2(\varphi_{xx} + \varphi_{yy}) \right. \\
&\left. - 2\varphi_{yz}\varphi_y\varphi_z - 2\varphi_{xz}\varphi_x\varphi_z - 2\varphi_{xy}\varphi_x\varphi_y \right]
\end{aligned} \tag{A3}
$$

and

$$
\begin{aligned}
G = \frac{1}{|\nabla\varphi|^4} &\left[\varphi_x^2(\varphi_{yy}\varphi_{zz} - \varphi_{yz}^2) + \varphi_y^2(\varphi_{xx}\varphi_{zz} - \varphi_{xz}^2) \right. \\
&+ \varphi_z^2(\varphi_{xx}\varphi_{yy} - \varphi_{xy}^2) - 2\varphi_x\varphi_y(\varphi_{xy}\varphi_{zz} - \varphi_{xz}\varphi_{yz}) \\
&- 2\varphi_x\varphi_z(\varphi_{xz}\varphi_{yy} - \varphi_{xy}\varphi_{yz}) \\
&\left. - 2\varphi_y\varphi_z(\varphi_{yz}\varphi_{xx} - \varphi_{xy}\varphi_{xz}) \right]
\end{aligned} \tag{A4}
$$

where φ was computed from ϕ in this study as follows:

$$\varphi = \sqrt{2}\eta \log\left(\frac{1 - \phi}{1 + \phi}\right) \tag{A2}$$

In Eqs. (A3) and (A4), φ_i and φ_{ij} represent the first and second derivatives of φ, respectively, with respect to the direction(s) denoted by the subscript.

References

[1] W. Kurz, M. Rappaz and R. Trivedi, Int. Mater. Rev., 66 (2021), 30.

[2] W.R. Fehlner, and S.H. Vosko, Can. J. Phys. 54 (1976) 2159.

[3] J.J. Hoyt, M. Asta, and A. Karma, Mater. Sci. Eng. R, 41 (2003), 121.

[4] T. Haxhimali, A. Karma, F. Gonzales, and M. Rappaz, Nat. Mater., 5 (2006), 660.

[5] L. Wang, J. J. Hoyt, N. Wang, N. Provatas, and C. W. Sinclair, Nat. Commun., 11(2020), 724.

[6] M. Ohno, Y. Oka, S. Sakane, Y. Shibuta, and T. Takaki, Phys. Rev. E, 101 (2020), 052121.

[7] R.E. Napolitano, and S. Liu, Phys. Rev. B, 70 (2004), 214103.

[8] J.J. Hoyt, M. Asta and A. Karma, Phys. Rev. Lett., 86 (2001), 5530.

[9] R.L. Davidchack and B.B. Laird, Phys. Rev. Lett., 85 (2000), 4751.

[10] Y. Nagatsuma, M. Ohno, T. Takaki and Y. Shibuta, Nanomaterials, 11 (2021), 2308.

[11] R. H. Mathiesen, L. Arnberg, F. Mo, T. Weitkamp and A. Snigirev, Phys. Rev. Lett., 83 (1999), 5062.

[12] H. Yasuda, I. Ohnaka, K. Kawasaki, A. Sugiyama, T. Ohmichi, J. Iwane and K. Umetani, J. Cryst. Growth, 262 (2004), 645.

[13] B. Billia, H. Nguyen-Thi, N. Mangelinck-Noel, N. Bergeon, H. Jung, G. Reinhart, A. Bogno, A. Buffet, J. Hartwig, J. Baruchel and T. Schenk, ISIJ Int., 50 (2010), 1929.

[14] T. M. Wang, J. J. Xu, T. Q. Xiao, H. L. Xie, J. Li, T. J. Li and Z. Q. Cao, Phys. Rev. E, 81 (2010), 042601.

[15] H. Yasuda, K. Morishita, N. Nakatsuka, T. Nishimura, M. Yoshiya, A. Sugiyama, K. Uesugi and A. Takeuchi, Nat. Commun., 10 (2019), 3183.

[16] N. Limodin, L. Salvo, E. Boller, M. Suéry, M. Felberbaum, S. Gailliègue and K. Madi, Acta Mater., 57 (2009), 2300.

[17] J. L. Fife, J. W. Gibbs, E. B. Gulsoy, C. -L. Park, K. Thornton and P. W. Voorhees, Acta Mater., 70 (2014), 66.

[18] J. W. Gibbs, K. A. Mohan, E. B. Gulsoy, A. J. Shahani, X. Xiao, C. A. Bouman, M. De Graef and P. W. Voorhees, Sci. Rep., 5 (2015), 11824.

[19] B. Cai, J. Wang, A. Kao, K. Pericleous, A. B. Phillion, R. C. Atwood and P. D. Lee, Acta Mater., 117 (2016), 160.

[20] R. Yamada, M. Kudo, G. Kim, T. Takaki, Y. Shibuta and M. Ohno, Comput. Mater. Sci., 204 (2022), 111173.

[21] I. Steinbach: Modell. Simul. Mater. Sci. Eng., 17 (2009), 073001.

[22] T. Takaki: ISIJ Int., 54 (2014), 437.

[23] A. Karma and D. Tourret, Curr. Opin. Solid State Mater. Sci., 20 (2016), 25.

[24] A. Karma and W. J. Rappel, Phys. Rev. Lett., 77 (1996), 4050.

[25] A. Karma, Phys. Rev. Lett., 87 (2001), 115701.

[26] M. Ohno and K. Matsuura, Phys. Rev. E, 79 (2009), 031603.

[27] M. Ohno and K. Matsuura, Acta Mater., 58 (2010), 5749.

[28] M. Ohno, Phys. Rev. E, 86 (2012), 051603.

[29] M. Ohno, T. Takaki and Y. Shibuta, Phys. Rev. E, 96 (2017), 033311.

[30] M. Ohno, ISIJ Int., 60 (2020), 2745.

[31] K. Glasner, J. Comput. Phys., 174 (2001), 695.

[32] J.J. Koenderink, and A.J. van Doorn, Image Vis. Comput., 10 (1992), 557.

[33] R. Yamashita, M. Nishio, R. K. G. Do, and K. Togashi, Insights Imaging, 9 (2018), 611.

[34] R. Kondo, S. Yamakawa, Y. Masuoka, S. Tajima, and R. Asahi, Acta Mater., 141 (2017), 29.

[35] S.M. Azimi, D. Britz, M. Engstler, M. Fritz, and F. Mücklich, Sci. Rep., 8 (2018), 2128.

[36] G. Kim, T. Takaki, Y. Shibuta, S. Sakane, K. Matsuura and M. Ohno, Comput. Mater. Sci., 162 (2019), 76.

[37] J.W. Gibbs, P.W. Voorhees, Integr. Mater. Manuf. Innov. 3 (1992) 557.

Table 1. Relative and absolute errors for ϵ_1 and ϵ_2.

	Error(ε_1), %	Error(ε_2), %	$\lvert\varepsilon_1-\varepsilon_1{}^{\text{est}}\rvert$	$\lvert\varepsilon_2-\varepsilon_2{}^{\text{est}}\rvert$
49 sets	7.163	15.029	3.32x10^{-3}	4.80x10^{-4}
100 sets	5.001	10.426	2.29x10^{-3}	3.16x10^{-4}
196 sets	3.287	5.470	1.45x10^{-3}	1.91x10^{-4}
400 sets	2.628	4.251	1.17x10^{-3}	1.42x10^{-4}

(a) Curvedness representation

(b) Shape factor representation
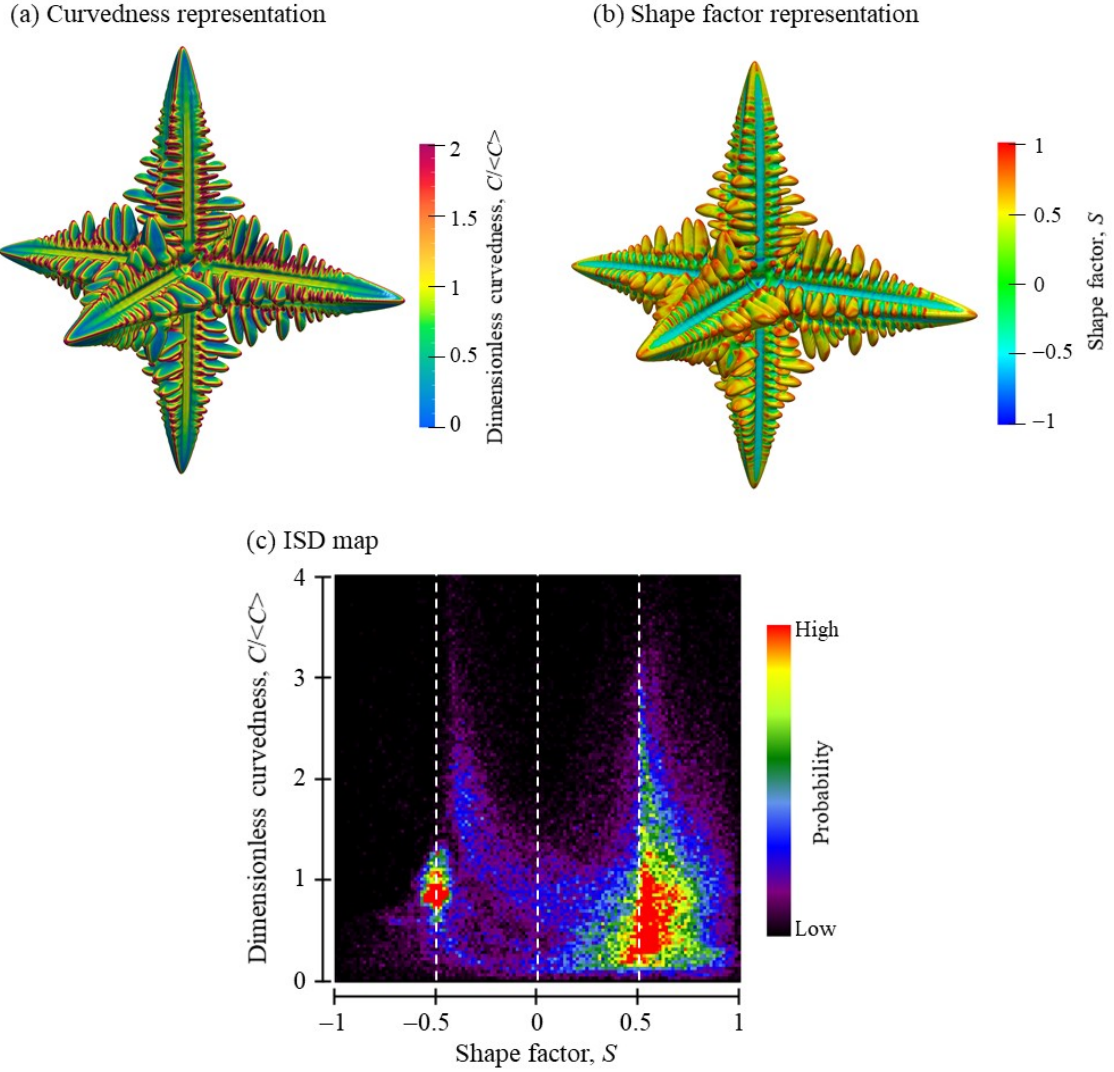
(c) ISD map

Fig. 1. (a,b) 3D dendrite structure and (c) the corresponding ISD map at $t = 40{,}000\Delta t$ simulated for $(\epsilon_1, \epsilon_2) = (0.1, 0)$. The local interface of the dendrite is colored according to the values of (a) $C/\langle C \rangle$ and (b) S.
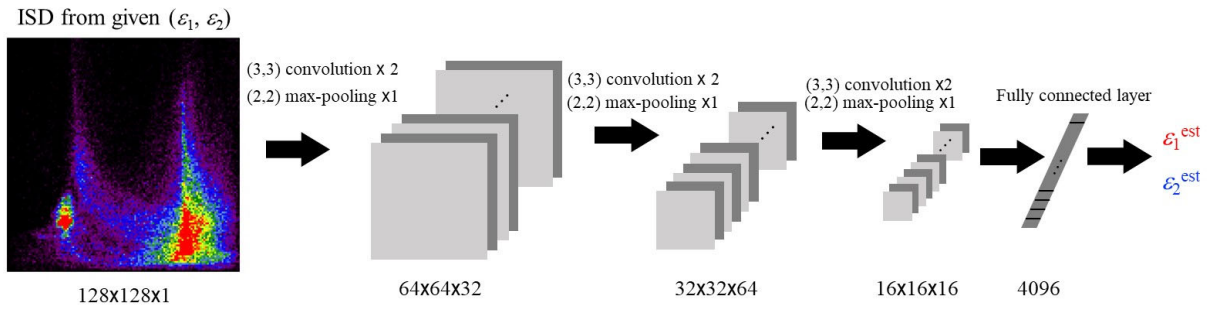
Fig. 2. CNN architecture used in this study. All convolution operations were performed with zero-padding and 1 stride and max-pooling was performed with 1 stride.
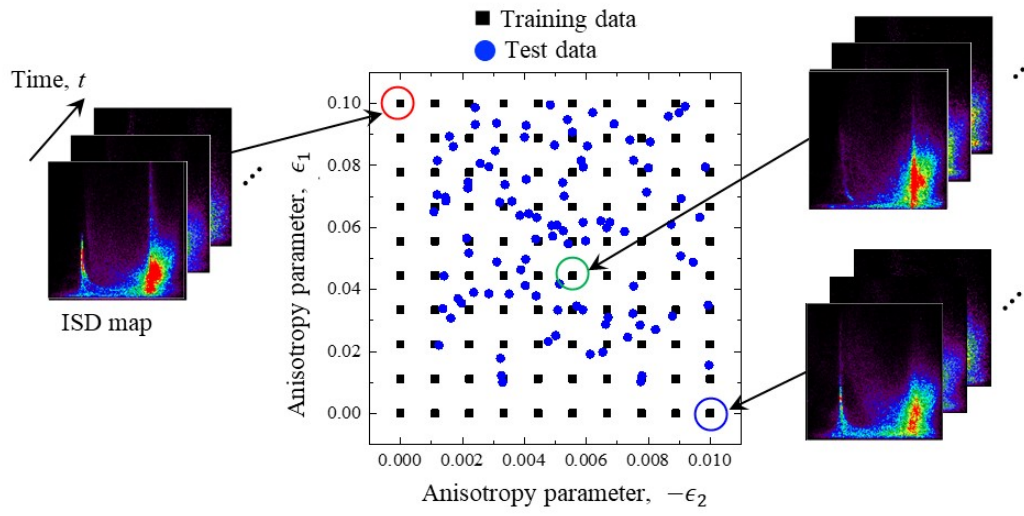
Fig. 3. Illustration of sampling the training and test datasets in the $\epsilon_1 - \epsilon_2$ space.
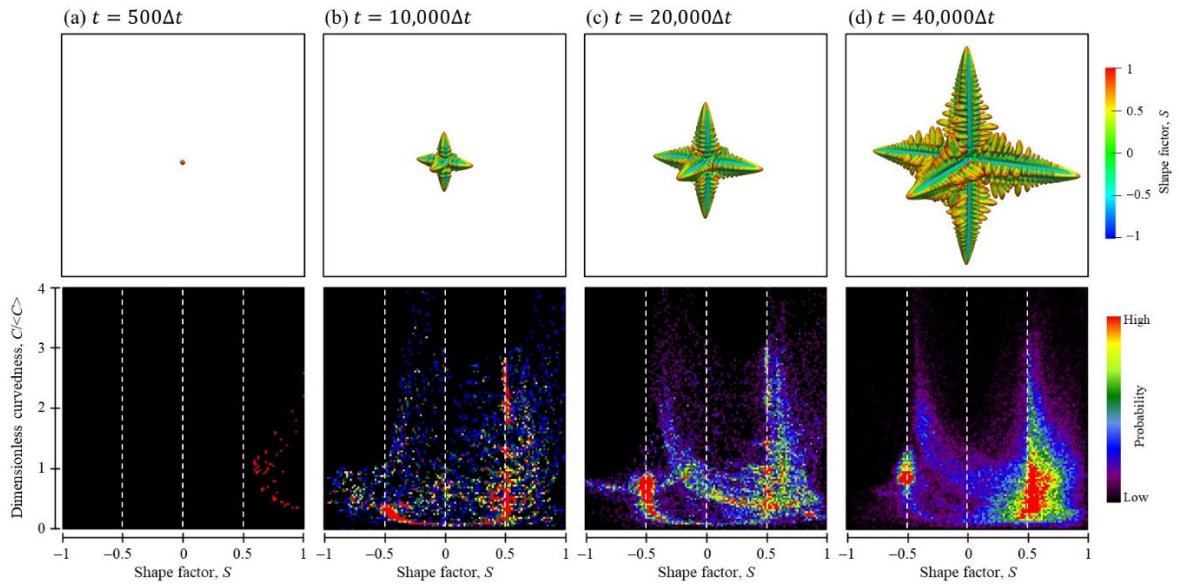
Fig. 4. Time evolution processes of the dendrite structure (upper) and corresponding ISD map (lower) for $(\epsilon_1, \epsilon_2) = (0.1, 0)$.
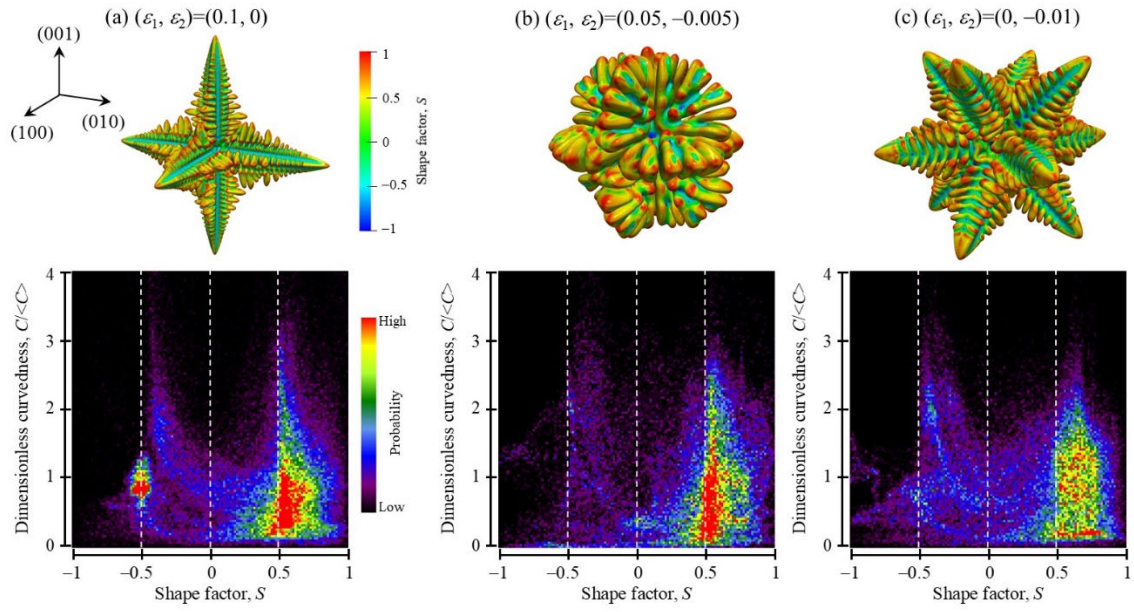
Fig. 5. Dendrite structures (upper) and ISD maps (lower) at $t = 40,000\Delta t$ in (a) <100>, (b) hyperbranched, and (c) <110> growth modes.
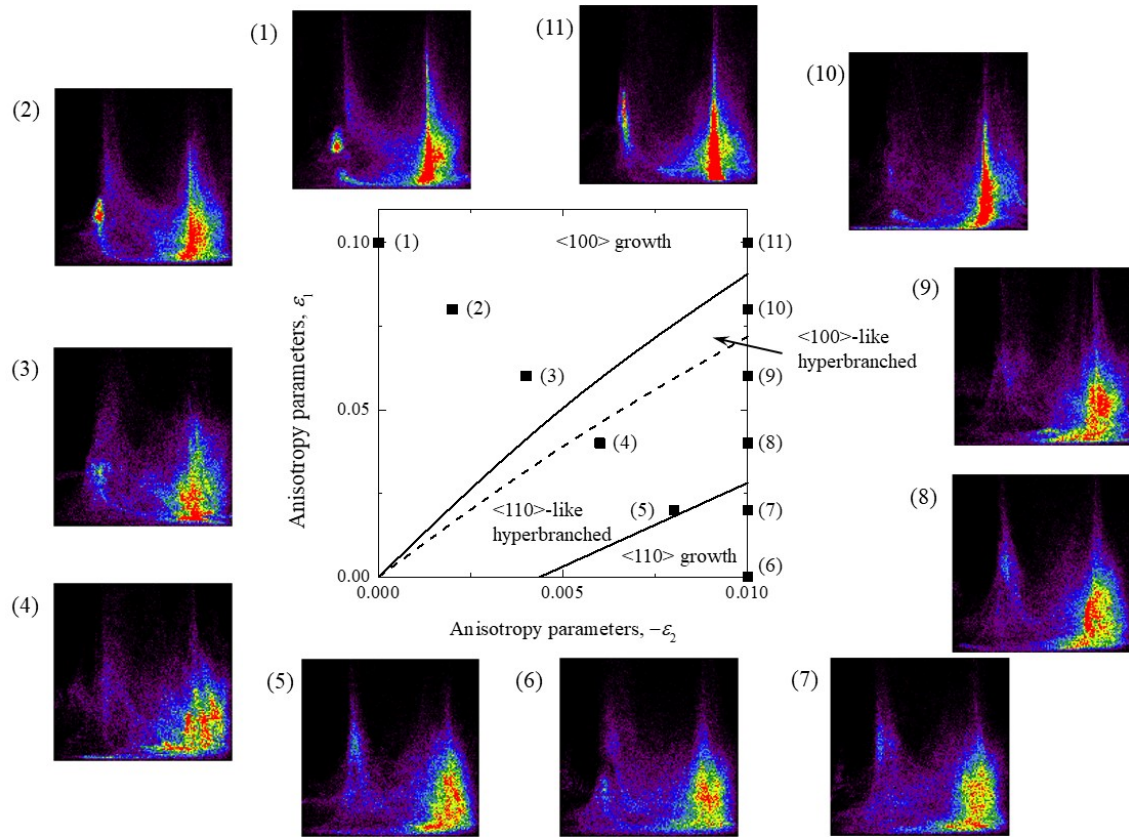
Fig. 6. ISD maps at $t = 40,000\Delta t$ for different values of ϵ_1 and ϵ_2 indicated in the orientation selection map.
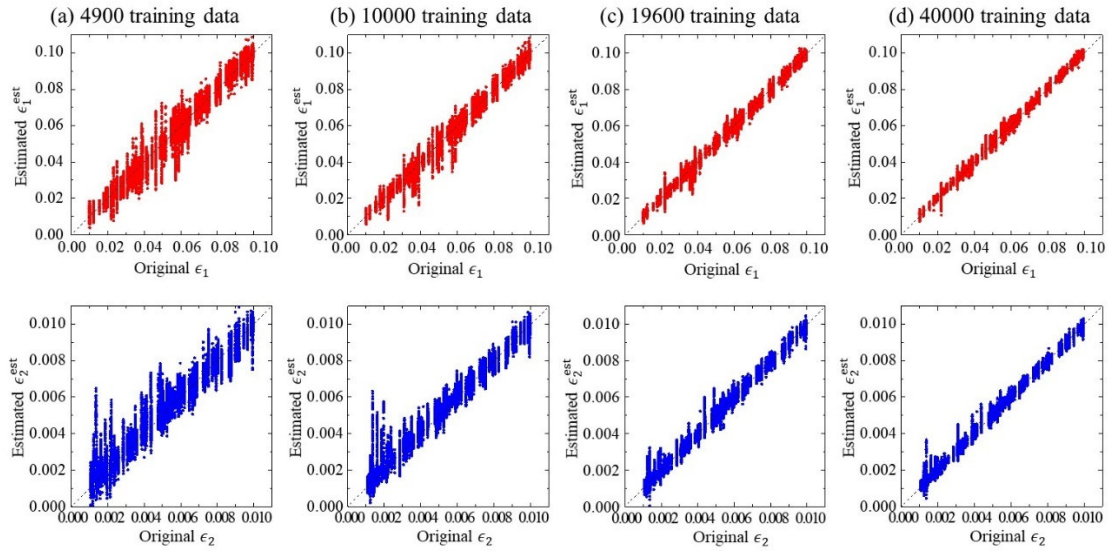
Fig. 7. Results of estimations of ϵ_1 and ϵ_2 obtained for different training datasets.
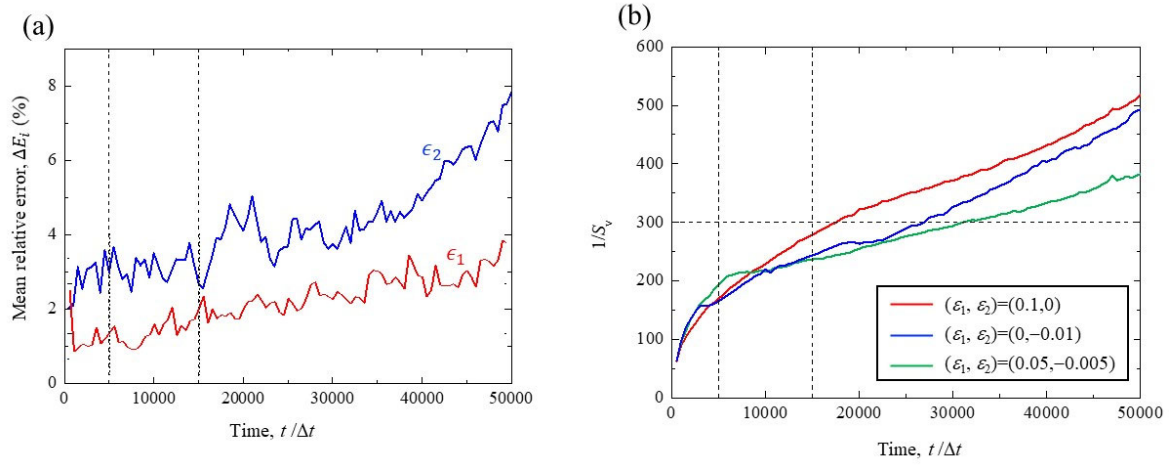
Fig. 8. Time changes of the (a) mean relative errors of ϵ_1 and ϵ_2 for the training dataset with 40000 maps and (b) reciprocal of the surface area per unit volume of the solid phase for different anisotropy parameters.